PHYSICAL REVIEW APPLIED **7,** 064035 (2017)

Hybrid Circuits with Nanofluidic Diodes and Load Capacitors

P. Ramirez,[1,*] V. Garcia-Morales,[1] V. Gomez,[1] M. Ali,[2,3] S. Nasir,[3] W. Ensinger,[2,3] and S. Mafe[4]
[1]*Departament de Física Aplicada, Universitat Politècnica de València, E-46022 València, Spain*
[2]*Department of Material- and Geo-Sciences, Materials Analysis, Technische Universität Darmstadt, D-64287 Darmstadt, Germany*
[3]*Materials Research Department, GSI Helmholtzzentrum für Schwerionenforschung, D-64291 Darmstadt, Germany*
[4]*Departament de Física de la Terra i Termodinàmica, Universitat de València, E-46100 Burjassot, Spain*
(Received 29 March 2017; revised manuscript received 26 May 2017; published 30 June 2017)

The chemical and physical input signals characteristic of micro- and nanofluidic devices operating in ionic solutions should eventually be translated into output electric currents and potentials that are monitored with solid-state components. This crucial step requires the design of hybrid circuits showing robust electrical coupling between ionic solutions and electronic elements. We study experimentally and theoretically the connectivity of the nanofluidic diodes in single-pore and multipore membranes with conventional capacitor systems for the cases of constant, periodic, and white-noise input potentials. The experiments demonstrate the reliable operation of these hybrid circuits over a wide range of membrane resistances, electrical capacitances, and solution pH values. The model simulations are based on empirical equations that have a solid physical basis and provide a convenient description of the electrical circuit operation. The results should contribute to advance signal transduction and processing using nanopore-based biosensors and bioelectronic interfaces.

DOI: 10.1103/PhysRevApplied.7.064035

I. INTRODUCTION

Micro- and nanofluidic devices operating in ionic solutions allow a wide range of functionalities because of the different pore-surface functionalizations currently available [1–4]. The interaction between the ions and the specific molecules functionalized on the pore surface of these soft nanostructures can be externally modulated by means of thermal, chemical, electrical, and optical signals [1–4]. The different nature of these input signals is crucial in applications such as electrochemical energy conversion, logic responses in sensors and actuators, and signal processing in bioelectrical interfaces [1,5–7]. However, to achieve full functionality, the physical responses at the nanoscale should eventually be translated into electric current and potential signals that are monitored with solid-state components. Therefore, significant physical advances require an efficient electrical coupling between the nanofluidic devices and conventional electronic elements such as capacitors in hybrid circuits.

We have studied recently the conversion of white-noise, zero average electrical potentials into net currents by using single nanofluidic diodes [8] and protein ion channels [9]. To check further the connectivity between these liquid-state nanostructures and conventional capacitor systems, we propose now to study experimentally and theoretically some fundamental theorems concerning energy conversion and charge transfer in hybrid networks.

The experimental results concern single-pore and multipore membranes and show the reliable operation of circuits where different load capacitors are interconnected with soft nanostructures that act as potential-dependent resistances. We propose also a physically motivated empirical equation for the current-voltage curves of the nanofluidic diodes that permits the analysis of hybrid circuits similar as in the case of conventional solid-state circuits. For the sake of generality, we use constant, periodic, and white-noise input potential signals. The membrane resistances are between 1 kΩ and 1 GΩ and the capacitances of the load capacitors vary between 10 nF and 10 mF. The electrolyte solution properties cover a wide range of pH values between 1 and 9, approximately. Because of the wide range of physical and chemical conditions considered, the experimental and theoretical results should contribute to advance signal transduction and processing using nanopore-based biosensors and bioelectronic interfaces [1,5,7–10].

II. EXPERIMENTAL METHODS

A. Nanofluidic diode fabrication

We use membrane samples with 1 and 10^4 tracks per cm^2 obtained from stacks of 12.5-μm-thick polyimide (PI) foils (Kapton50 HN, DuPont) irradiated with swift heavy ions (Au) of energy 11.4 MeV per nucleon under normal incidence at the linear accelerator UNILAC (GSI, Darmstadt). Under these conditions, the range of heavy

---

[*] patraho@fis.upv.es

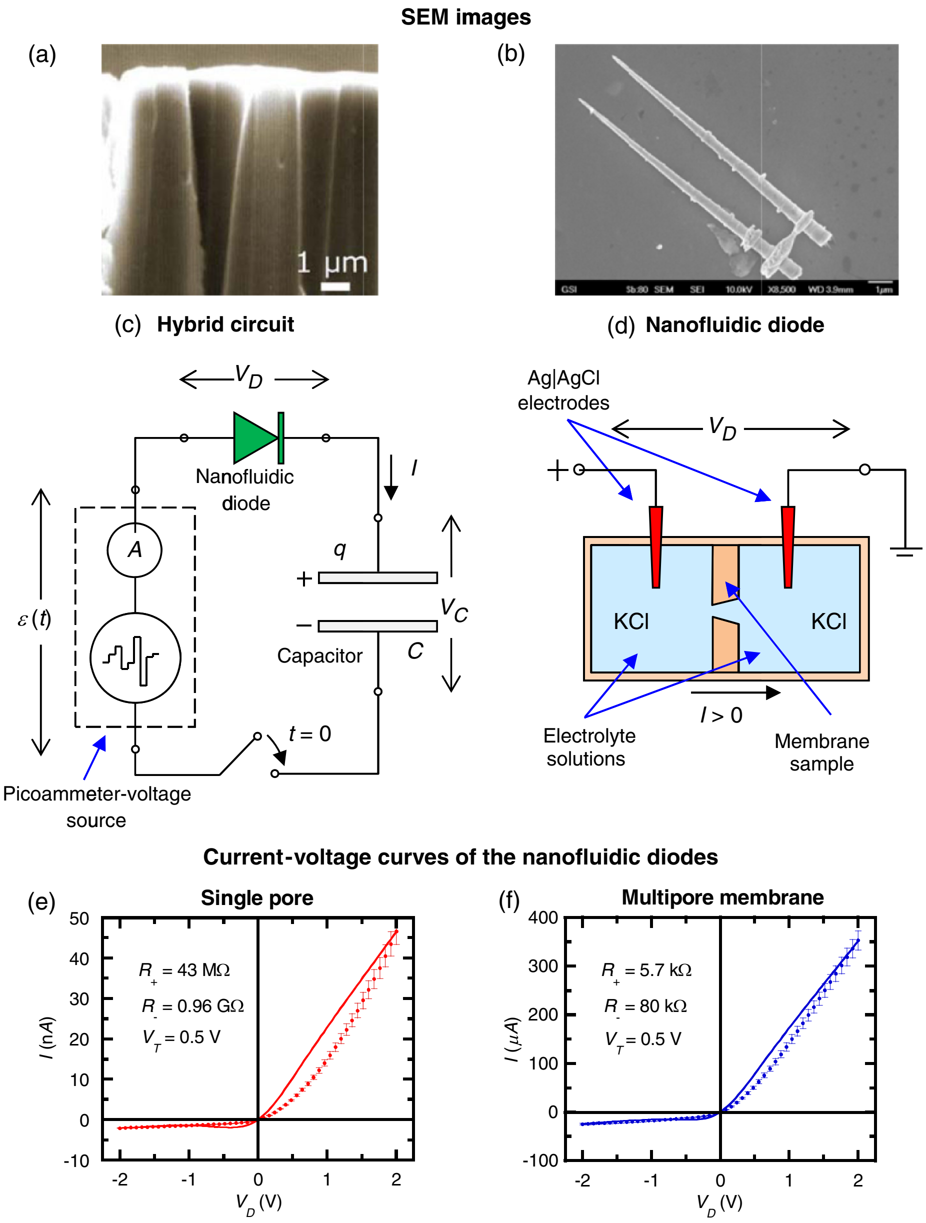

FIG. 1. SEM images (a) and gold replicas (b) of the conical nanopores obtained by track etching. Hybrid circuit with the nanofluidic diode and the load capacitor (c). Electrochemical cell with the nanofluidic diode (d). Typical current-voltage curves obtained for the single-pore (e) and multipore (f) membranes obtained at $p\mathrm{H} = 6.6$. The continuous curves represent the current-voltage curves obtained using Eq. (1) with the model parameters shown in the inset.

ions in PI is larger than the thickness of the six-foil stack so that the energy loss of the ions is above the threshold required for homogeneous track etching. In front of each stack, a metal mask with a 200-μm-diameter centered aperture is placed for the case of single-ion irradiation. As soon as a single ion passes through the foil stack and is registered by a particle detector behind the samples, the ion beam is blocked. The procedure gives tracks in the membrane that are converted into approximately conical pores by asymmetric track-etching techniques [11,12]. Figure 1(a) shows a SEM image of the fracture for a multipore membrane sample that is overexposed to better show the pore characteristics, and Fig. 1(b) shows gold replicas of the conical pores obtained. The typical pore radii range from 10–40 nm (cone tip) to 300–600 nm (cone base) [12]. The track-etching processes yield carboxylate residues on the pore surface that eventually result in fixed charges when the membrane is exposed to aqueous ionic solutions of KCl and different pH values. The sign of these charges depends on the solution pH, and the approximately conical pore geometry is responsible for the electrical rectification characteristic of the nanofluidic diodes [11–17].

B. Electrical measurements

Figure 1(c) shows a scheme of the hybrid circuit. The picoammeter-voltage source (Keithley 6487/E) provides the input potential $\varepsilon(t)$ and controls the current I through the circuit obtained upon closing the switch at time $t = 0$. The potential drops across the nanofluidic diode (V_D) and the load capacitor (V_C) of capacitance C are measured with a multimeter (Keithley 2000/E). Figure 1(d) shows a scheme of the electrochemical cell with the nanofluidic diode for the single-pore-membrane case. The membrane area exposed to the aqueous ionic solutions is 1 cm^2. The membrane samples are bathed by 0.1-M KCl electrolyte solutions under controlled-pH conditions. Ag|AgCl electrodes immersed in the bathing solutions are employed to introduce the input potentials in the electrochemical cell and measure the electric currents. Note the sign criteria used for voltages and currents.

Figures 1(e) and 1(f) show typical current-voltage (I-V_D) curves obtained for the single-pore and multipore membranes, respectively. The curves show current rectification characteristics: low pore resistances are obtained when the current enters the cone tip ($V_D > 0$), while high resistances are observed when the current enters the cone base ($V_D < 0$). The reproducibility of the nanopore I-V_D curves and the membrane responses is checked several times in all experiments conducted with the different circuits, and the resulting error bars are included in Figs. 1(e) and 1(f).

III. MODEL

Ionic transport processes through conical nanopores have been studied intensively during the past decade [1,3,12–17]. Most of the proposed models are based on the Poisson-Nernst-Planck equations that allow for the calculation of the I-V_D curves in terms of the pore geometry, the surface concentration of the fixed charges, and the concentrations and the diffusion coefficients of the electrolyte ions [12,17]. Although these models provide an accurate description of single pores, the calculations involve complicated numerical schemes which make this approach unsuitable for the practical analysis of hybrid circuits composed of multiple interconnected elements. As a simplified alternative, we propose here a physically motivated empirical equation for $I(V_D)$:

$$I = \frac{V_D}{2rR_+}\left[r + 1 + (r-1)\tanh\left(\frac{V_D}{V_T}\right)\right], \qquad (1)$$

where $r \equiv R_-/R_+$ is the ratio of the resistances R_+ and R_- experimentally observed for high positive and negative voltages, respectively. For high positive V_D, Eq. (1) gives $I \approx V_D/R_+$ asymptotically, while for high negative voltages V_D, it reduces to $I \approx V_D/R_-$ The parameter V_T describes the electrical sharpness of the transition between these two Ohmic regimes. The continuous lines in Figs. 1(e) and 1(f) are the results obtained from Eq. (1) using the parameters shown in the inset. This approach should be valid for not too high voltages and allows for the use of standard methods of circuit analysis while keeping the number of free parameters to a minimum. In addition, the use of Eq. (1) permits us to obtain quantitative predictions for the hybrid circuits described in the following section.

IV. RESULTS AND DISCUSSION

Figures 2(a) and 2(b) schematically show the charging (time $t = 0$) and discharging (time $t = t_s$) circuits for two nanofluidic diode configurations together with the experimental curves obtained at the constant input potential $\varepsilon = 2$ V for single-pore [Figs. 2(c) and 2(d)] and multipore [Figs. 2(e) and 2(f)] membranes. In Figs. 2(c) and 2(e), the charging of capacitor 1 proceeds through the nanodiode high-conductive polarity, while the charge transfer to capacitor 2 occurs through the low-conductive polarity. The opposite case is considered in Figs. 2(d) and 2(f). As in the conventional resistor-capacitor circuit (RC circuit), the capacitor voltage V_{C1} eventually reaches the source voltage. Upon the discharge to capacitor 2, half of the energy initially stored in capacitor 1 is finally stored in capacitor 2, regardless of the particular nanodiode resistance characteristic of the charge-transfer process. The time constants of the RC circuits of Figs. 2(a) and 2(b) are shown in Table I for the charging experiments of Figs. 2(c)–2(f). For the charge transfer, the final voltage of capacitors is $V_{\mathrm{st}} = C_1V/(C_1 + C_2)$ and then the dissipated energy is $(1/2)\varepsilon^2C_1C_2/(C_1 + C_2)$, regardless of the particular nanodiode resistance characteristic of the process. The time constants of the RC circuits of Figs. 2(a) and 2(b) are shown in Table II for the charge-transfer experiments of Figs. 2(c)–2(f). Note the excellent agreement between the theoretical steady-state voltages V_{st} and the experimental saturation voltages of Figs. 2(c)–2(f). This is also the case of the theoretical and experimental time constants.

Figure 3(a) considers the case of a periodic input signal of zero average and the multipore membrane for the charging circuit of Fig. 1(c). The sinusoidal signal of amplitude of 2 V has a period of 105 s. Because of the electrical rectification, the capacitor is charged with time. For high enough capacitances, the oscillating capacitor voltage attains an average value which is independent of the capacitance. On the contrary, the charging time constant increases with this capacitance, while the oscillation amplitude decreases with the capacitance. Figure 3(b) shows the I-ε curve for the circuit of Fig. 1(c). The experimental loop gives the minimum and maximum values of the capacitor voltage V_C defined by the condition of zero current, $I = 0$.

The time evolution of the potential V_C across the capacitor is governed by the equation $CdV_C/dt = I$, where I is the current of Eq. (1). This differential equation can be discretized for small time steps Δt to give $V_{C,t+1} = V_{C,t} + \Delta t\, I/C$, where the second subscript makes reference to time. Since the voltage across the nanofluidic diode can be written as $V_D = \varepsilon - V_C$, Eq. (1) gives

$$V_{C,t+\Delta t} = V_{C,t} + \Delta t\frac{\varepsilon - V_{C,t}}{\tau_{\mathrm{ch}}}\left[1 + \frac{r-1}{r+1}\tanh\left(\frac{\varepsilon - V_{C,t}}{V_T}\right)\right], \qquad (2)$$

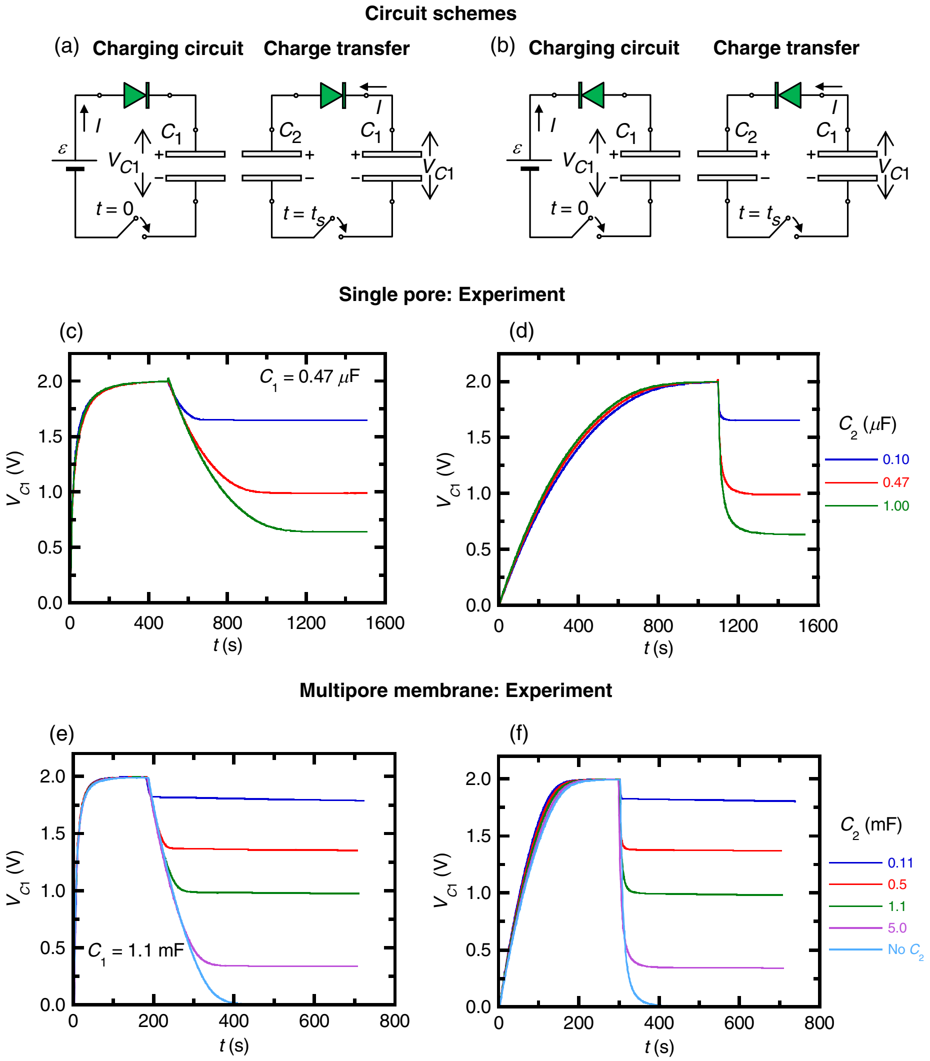

FIG. 2. The charging and discharging (charge transfer between capacitors) circuits for two nanofluidic diode configurations (a) and (b). Experimental curves measured for single-pore membrane [(c) and (d)]. The curves correspond to $C_2 = 0.10$, 0.47, and 1.0 μF, from top to bottom. Experimental curves measured for multipore membrane [(e) and (f)]. The curves correspond to $C_2 = 0.11$, 0.5, 1.1, 5.0, and 0 mF, from top to bottom. All curves are obtained with constant input potential $\varepsilon = 2$ V.

where we introduce the characteristic time $\tau_{\mathrm{ch}} \equiv [2r/(r+1)]R_+C$. Figures 3(c) and 3(d) show that the theoretical curves obtained with Eq. (2) are in good agreement with the experiments. The small differences between the theoretical and the experimental curves arise from the approximated equation used for $I(V_D)$ [see Figs. 1(e) and 1(f)].

Figure 4 shows the case of the white-noise input signal for single-pore [Figs. 4(a) and 4(b)] and multipore [Figs. 4(c) and 4(d)] membranes. This case is of interest for energy transduction using external noisy signals [8,9]. As observed previously in the case of the periodic input signal (Fig. 3), the limiting value of the capacitor voltage does not change with the capacitance [see Figs. 4(a)–4(c)], which is not the case of the time constants and the fluctuating potential amplitudes around the average potential. The theoretical results of Fig. 4(b) are obtained introducing in Eq. (2) a voltage ε_t that takes random values in the interval $[-V_0, V_0]$ at each time step according to a uniform distribution. Figure 4(d) shows the I-ε curve for the circuit of Fig. 1(c) in the case of the multipore membrane. The minimum and maximum values of the capacitor voltage V_C are now approximately described by the condition of zero current, $I = 0$. The amplitude between the extreme values of Fig. 4(d) approximately corresponds to the difference between the minimum and maximum fluctuating potentials of Fig. 4(c).

TABLE I. Time constants for the *RC* circuits of Figs. 2(a) and 2(b) in the charging experiments of Figs. 2(c)–2(f).

	Time constant (s)	
	Circuit *a*	Circuit *b*
Single pore	20 ± 3	450 ± 60
Multipore membrane	6.3 ± 0.6	88 ± 12

Figure 5 considers the effect of the solution properties (pH) on the I-V_D curves [Fig. 5(a)], the charging process [Figs. 5(b) and 5(c)], and the dependence of the steady-state voltage V_{st} on the rectification ratio r [Fig. 5(d)]. Note the effect of the pore fixed-charge sign on the I-V_D curves: decreasing the pH causes a decrease in the negative surface charge density and eventually reverses it to give a positive

TABLE II. Time constants, theoretical steady-state voltages V_{st}, and capacitances of the *RC* circuits in Figs. 2(a) and 2(b) for the charge-transfer experiments of Figs. 2(c)–2(f).

			Time constant (s)	
	C_2 (μF)	V_{st} (V)	Circuit *a*	Circuit *b*
Single pore	0.10 ± 0.01	1.65 ± 0.04	79 ± 9	3.5 ± 0.5
	0.47 ± 0.05	1.00 ± 0.07	230 ± 30	10.1 ± 0.9
	1.0 ± 0.1	0.64 ± 0.06	300 ± 30	13.7 ± 0.9
	C_2 (mF)	V_{st} (V)	Circuit *a*	Circuit *b*
Multipore membrane	0.11 ± 0.01	1.82 ± 0.02	8.0 ± 0.9	0.57 ± 0.08
	0.50 ± 0.05	1.38 ± 0.06	28 ± 4	2.0 ± 0.3
	1.1 ± 0.1	1.00 ± 0.07	44 ± 8	3.1 ± 0.4
	5.0 ± 0.5	0.36 ± 0.04	72 ± 10	5.2 ± 0.8
	No capacitor	0	88 ± 12	6.3 ± 0.6

charge density [12,13]. This experimental fact changes the sign of the voltage V_C in Figs. 5(b) (experiment) and 5(c) (model). Table III gives the different membrane resistances obtained from Fig. 5(a) together with the experimental [Fig. 5(b)] and theoretical [Fig. 5(c)] steady-state voltages as a function of the solution *p*H. These results provide a direct comparison between the experimental data and the model results. The results of Table III suggest that the model predictions can give a quantitative description of the experiments.

We use now the theoretical model to analyze the experimental results of Figs. 4 and 5. By introducing $t = n\Delta t$ with n a non-negative integer, we can obtain the time average of a generic magnitude f_t over a long time $T = N\Delta t$ as

$$\langle f_t \rangle = \frac{\Delta t}{T} \sum_{n=0}^{N-1} f_{n\Delta t}. \tag{3}$$

Note that we have $\langle \varepsilon_t \rangle = 0$ because the applied voltage is uniformly distributed. When the capacitor potential reaches a stationary state, $\langle V_{C,t} \rangle = V_{\mathrm{st}}$, with $\xi_t = V_{C,t} - V_{\mathrm{st}}$, the deviation of the instantaneous capacitor potential from the

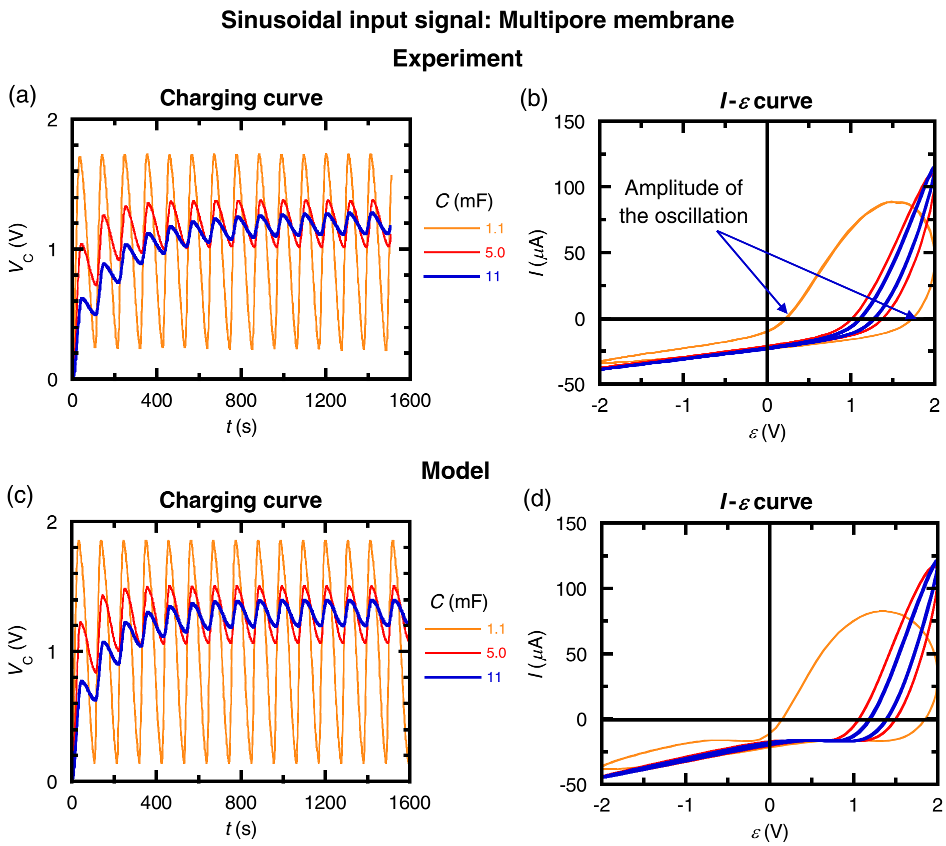

FIG. 3. Experiments with a periodic input signal (sinusoidal wave) of zero average and the multipore membrane [(a) and (b)]. Theoretical curves obtained with Eq. (2) [(c) and (d)].

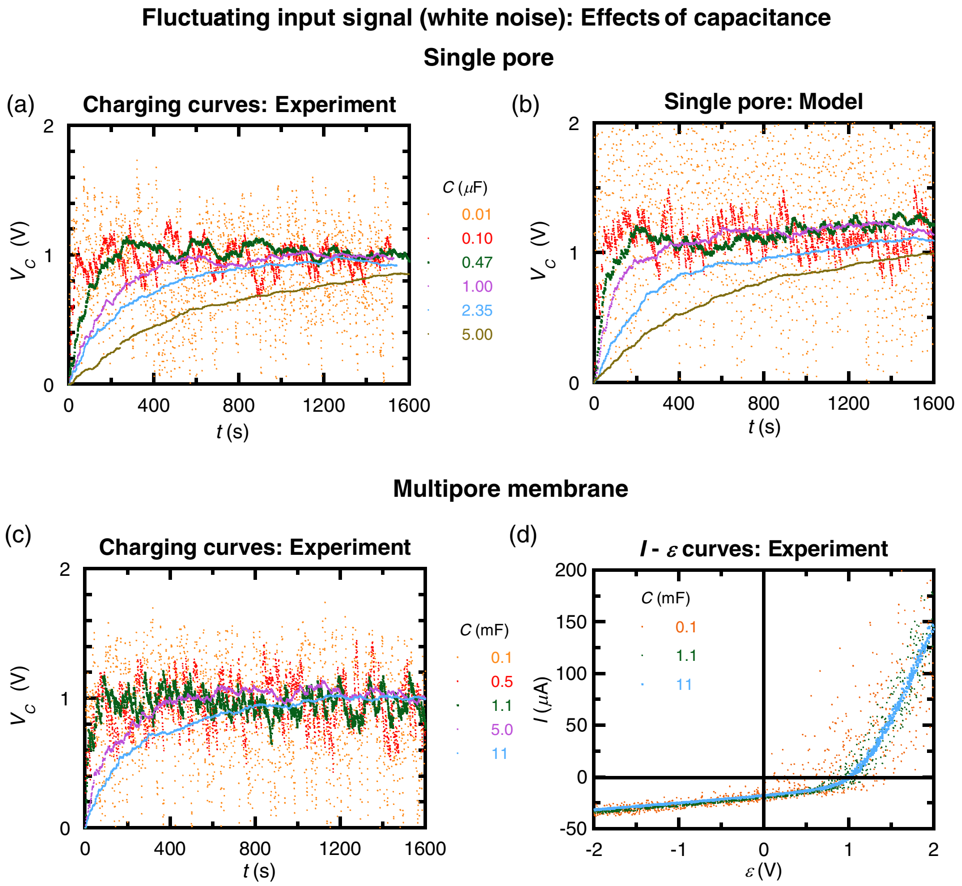

FIG. 4. Experiments with white-noise input signals for single-pore (a) and multipore membranes [(c) and (d)]. Theoretical results obtained with Eq. (2) for the single pore (b). The highly scattered data correspond to the lowest capacitance.

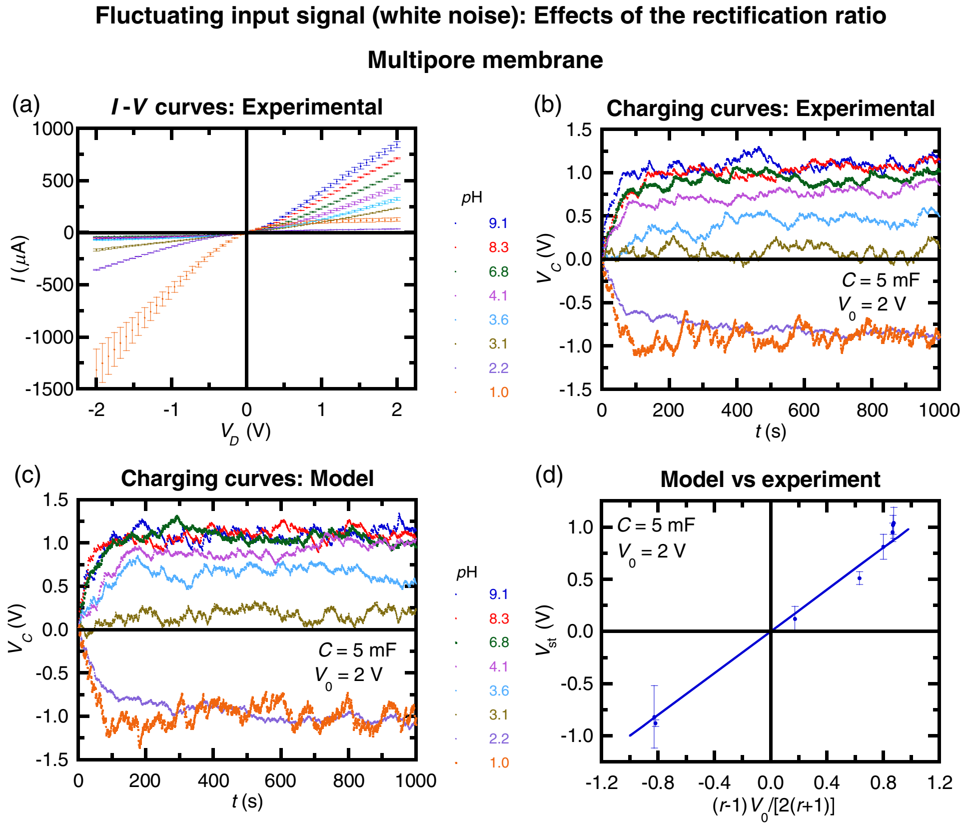

FIG. 5. Effect of the solution properties (pH) on the capacitor charging. Experimental current-voltage curves of the multipore membrane at different pH values and rectification ratios (a). Experimental charging curves of the capacitor at different pH values (b). Theoretical results obtained with Eq. (2) (c). The dependence of the steady-state voltage V_{st} on the rectification ratio r shows the agreement between the theoretical curve [Eq. (8)] and the experimental data (d). Error bars correspond to data obtained in three independent measurements.

TABLE III. Membrane resistances obtained from Fig. 5(a), experimental steady-state voltages obtained from Fig. 5(b), and theoretical steady-state voltages obtained from Fig. 5(c) as a function of the solution pH.

pH	R_+(kΩ)	R_-(kΩ)	$V_{\rm st}$ (V), exp	$V_{\rm st}$ (V), model
9.1	2.4 ± 0.1	35 ± 4	1.04 ± 0.15	1.10 ± 0.04
8.3	2.80 ± 0.03	40 ± 3	1.02 ± 0.09	1.09 ± 0.03
6.8	3.51 ± 0.04	49 ± 3	0.98 ± 0.10	1.01 ± 0.03
4.1	4.5 ± 0.2	41 ± 2	0.81 ± 0.12	0.92 ± 0.03
3.6	6.2 ± 0.3	27 ± 2	0.51 ± 0.06	0.56 ± 0.02
3.1	8.5 ± 0.1	12.0 ± 0.7	0.12 ± 0.12	0.18 ± 0.07
2.2	56 ± 2	5.60 ± 0.08	-0.98 ± 0.03	-0.96 ± 0.01
1.0	16 ± 2	1.5 ± 0.2	-0.92 ± 0.03	-0.90 ± 0.02

average stationary-state value, so that $\langle \xi_t \rangle = 0$. Therefore, we have from Eq. (2) that

$$0 = \left\langle \Delta t \frac{\varepsilon_t - \xi_t - V_{\rm st}}{\tau_{\rm ch}} \left[1 + \frac{r-1}{r+1} \tanh\left(\frac{\varepsilon_t - \xi_t - V_{\rm st}}{V_T}\right)\right] \right\rangle, \tag{4}$$

and then

$$V_{\rm st} = \frac{r-1}{r+1} \left\langle (\varepsilon_t - \xi_t - V_{\rm st}) \tanh\left(\frac{\varepsilon_t - \xi_t - V_{\rm st}}{V_T}\right) \right\rangle. \tag{5}$$

In the limit $V_T \to 0$, we obtain

$$V_{\rm st} = \frac{r-1}{r+1} \langle |\varepsilon_t - \xi_t - V_{\rm st}| \rangle. \tag{6}$$

For negligible small fluctuations $\xi_t \approx 0$, this equation reduces to

$$V_{\rm st} = \frac{r-1}{r+1} \langle |\varepsilon_t - V_{\rm st}| \rangle. \tag{7}$$

The average $\langle x \rangle$ of a stochastic variable x uniformly distributed in the interval $[a, b]$ is $\langle x \rangle = (a+b)/2$ and then $\langle |\varepsilon_t - V_{\rm st}| \rangle = V_0/2$ because $|\varepsilon_t - V_{\rm st}|$ is uniformly distributed in the interval $[V_0 - V_{\rm st}, V_0 + V_{\rm st}]$. Therefore, Eq. (7) becomes

$$V_{\rm st} = \left(\frac{r-1}{r+1}\right) \frac{V_0}{2}, \tag{8}$$

which shows that the average capacitor voltage depends linearly on the ratio $(r-1)/(r+1)$ and the maximum value V_0 of the applied voltage ε_t. Figure 5(d) shows that Eq. (8) can describe the experimental data obtained with the multipore membrane at several pH values.

In addition, Eq. (8) predicts that the average stationary voltage does not depend on the capacitor characteristics, as shown experimentally in Fig. 4. However, the amplitude of the fluctuations does depend on the capacitance through the characteristic time $\tau_{\rm ch}$. Indeed, if we take $\xi_t = 0$, Eq. (2) becomes

$$|\xi_{t+\Delta t}| = \left| \Delta t \frac{\varepsilon_t - V_{\rm st}}{\tau_{\rm ch}} \left[1 + \frac{r-1}{r+1} \tanh\left(\frac{\varepsilon_t - V_{\rm st}}{V_T}\right)\right] \right|, \tag{9}$$

which reduces to

$$|\xi_{t+\Delta t}| = \frac{\Delta t}{\tau_{\rm ch}} \left| \varepsilon_t - V_{\rm st} + \frac{r-1}{r+1} |\varepsilon_t - V_{\rm st}| \right| \tag{10}$$

in the limit $V_T \to 0$. For $r \geq 1$, the maximum value $|\xi|_{\rm max}$ of any fluctuation around the stationary state can be obtained from Eq. (10) with $\varepsilon_t = V_0$ and Eq. (8) as

$$|\xi|_{\rm max} = \frac{\Delta t}{\tau_{\rm ch}} \frac{r+3}{(r+1)^2} V_0. \tag{11}$$

Equation (11) shows that low capacitances give high fluctuations around the average voltage. Note also that $\tau_{\rm ch}$ is bounded below by Δt. If $r = 1$, $V_{\rm st} = 0$ from Eq. (8) and then $|\xi|_{\rm max} = (\Delta t / \tau_{\rm ch}) V_0$ from Eq. (11). Therefore, for small values of C, $|\xi|_{\rm max} \approx V_0$ and the signal becomes indistinguishable from the noisy applied voltage.

V. CONCLUSIONS

Fluidic devices operating in ionic solutions can be used to process a variety of chemical and physical signals. Input signals defined at the micro- and nanoscale should eventually be translated into electric currents and potentials that are monitored with solid-state components [1,5–7]. This crucial step requires the design of circuits showing robust electrical coupling between the ionic solutions and the electronic elements. We study experimentally and theoretically the connectivity between liquid-state nanofluidic diodes and conventional capacitors. Fundamental questions concerning energy conversion and charge transfer in hybrid networks are addressed. In particular, we show that the limiting value of the load capacitor voltage does not change with the capacitance for the different input signals used.

The experiments are conducted using single-pore and multipore membranes in the cases of constant, periodic, and white-noise input potential signals. The extension of the analysis to single-protein-ion channels [9] and square wave and triangular signals [14,15] can also be possible because of the robust rectification characteristics of the nanopores [12,16,17]. The membrane resistances, load capacitor capacitances, and solution pH values cover a wide range of experimental cases. The theoretical model is based on a semiempirical equation that provides a good description of the electrical circuit operation.

ACKNOWLEDGMENTS

We acknowledge the support from the Ministry of Economic Affairs and Competitiveness and FEDER (Project No. MAT2015-65011-P). M. A., S. N., and W. E. acknowledge the funding from the Hessen State Ministry of Higher Education, Research and the Arts, Germany, under the LOEWE project iNAPO.

[1] M. Tagliazucchi and I. Szleifer, Transport mechanisms in nanopores and nanochannels: Can we mimic nature?, Mater. Today **18**, 131 (2015).

[2] Q. Liu, L. Wen, K. Xiao, H. Lu, Z. Zhang, G. Xie, X.-Y. Kong, Z. Bo, and L. Jiang, A biomimetic voltage-gated chloride nanochannel, Adv. Mater. **28**, 3181 (2016).

[3] P. Ramirez, J. Cervera, M. Ali, W. Ensinger, and S. Mafe, Logic functions with stimuli-responsive single nanopores, ChemElectroChem **1**, 698 (2014).

[4] G. Pérez-Mitta, A. G. Albesa, C. Trautmann, M. E. Toimil-Molares, and O. Azzaroni, Bioinspired integrated nanosystems based on solid-state nanopores: "Iontronic" transduction of biological, chemical and physical stimuli, Chem. Sci. **8**, 890 (2017).

[5] N. Misra, J. A. Martinez, S.-C. J. Huang, Y. Wang, P. Stroeve, C. P. Grigoropoulos, and A. Noy, Bioelectronic silicon nanowire devices using functional membrane proteins, Proc. Natl. Acad. Sci. U.S.A. **106**, 13780 (2009).

[6] Y. Hou, R. Vidu, and P. Stroeve, Solar energy storage methods, Ind. Eng. Chem. Res. **50**, 8954 (2011).

[7] M. Ali, P. Ramirez, W. Ensinger, and S. Mafe, Information processing with a single multifunctional nanofluidic diode, Appl. Phys. Lett. **101**, 133108 (2012).

[8] V. Gomez, P. Ramirez, J. Cervera, S. Nasir, M. Ali, W. Ensinger, and S. Mafe, Charging a capacitor from an external fluctuating potential using a single conical nanopore, Sci. Rep. **5**, 9501 (2015).

[9] C. Verdia-Baguena, V. Gomez, J. Cervera, P. Ramirez, and S. Mafe, Energy transduction and signal averaging of fluctuating electric fields by a single protein ion channel, Phys. Chem. Chem. Phys. **19**, 292 (2017).

[10] O. Yehezkeli, R. Tel-Vered, J. Wasserman, A. Trifonov, D. Michaeli, R. Nechushtai, and I. Willner, Integrated photosystem II-based photo-bioelectrochemical cells, Nat. Commun. **3**, 742 (2012).

[11] P. Apel, Track etching technique in membrane technology, Radiation Measurements **34**, 559 (2001).

[12] M. Ali, P. Ramirez, S. Mafe, R. Neumann, and W. Ensinger, A *p*H-tunable nanofluidic diode with a broad range of rectifying properties, ACS Nano **3**, 603 (2009).

[13] J. Cervera, P. Ramirez, V. Gomez, S. Nasir, M. Ali, W. Ensinger, P. Stroeve, and S. Mafe, Multipore membranes with nanofluidic diodes allowing multifunctional rectification and logical responses, Appl. Phys. Lett. **108**, 253701 (2016).

[14] V. Gomez, P. Ramirez, J. Cervera, S. Nasir, M. Ali, W. Ensinger, and S. Mafe, Converting external potential fluctuations into nonzero time-average electric currents using a single nanopore, Appl. Phys. Lett. **106**, 073701 (2015).

[15] E. Kalman, K. Healy, and Z. S. Siwy, Tuning ion current rectification in asymmetric nanopores by signal mixing, Europhys. Lett. **78**, 28002 (2007).

[16] Z. Siwy, I. D. Kosińska, A. Fuliński, and C. R. Martin Asymmetric Diffusion through Synthetic Nanopores, Phys. Rev. Lett. **94**, 048102 (2005).

[17] Z. S. Siwy and S. Howorka, Engineered voltage-responsive nanopores, Chem. Soc. Rev. **39**, 1115 (2010).